CMS Physics Analysis Summary

Contact: cms-pag-conveners-higgs@cern.ch 2013/07/01

Properties of the observed Higgs-like resonance decaying into two photons

The CMS Collaboration

Abstract

Analyses are reported on properties of the recently discovered Higgs-like resonance around 125 GeV in its decay to two photons. The analyses are performed using the 2011 (2012) dataset recorded by the CMS experiment at the LHC from pp collisions at a centre-of-mass energy of 7 (8) TeV. The dataset corresponds to an integrated luminosity of 5.1 (19.6) fb^{-1}. The spin analysis is evaluated on the 2012 dataset alone. An upper limit on the natural width of the observed resonance is found to be 6.9 GeV at 95% confidence level. A search has been performed for second Higgs-like states in the range $110 < m_H < 150$ GeV. Spin hypothesis tests have been performed comparing the Standard Model Higgs with a spin-2 graviton-like model with minimal couplings. The current data cannot exclude this particular model of spin-2 whilst the data are compatible with the Standard Model Higgs at the 1σ level.

1 Introduction

After the observation of a Higgs-like boson at around 125 GeV by both the ATLAS and CMS experiments [1, 2] it has become important to measure the state's properties and quantum numbers to determine whether they are compatible with predictions from the standard model (SM) [3–8].

We present details of measurements made on the observed resonance decaying into two photons. Firstly, we reinterpret the data with models that allow:

- setting a limit on the natural width of the new state,
- looking for a second Higgs-like boson elsewhere, in the mass range $110 < m_H < 150$, by treating the observed signal at m_{H}=125 GeV as background,
- testing the possibility that the observed signal could be a superposition of two states quasi-degenerate in mass.

These are simple extensions of the SM analysis documented in Ref. [9], using the same event selection, categorisation and model parametrisation, but with additional terms in the likelihood to extract values and set limits on the relevant new quantities.

Secondly, in the context of the SM, we use hypothesis tests to study the compatbility of different spin models with the observed resonance. This analysis uses a simplified, cut-based analysis focused on separating spin models in as model independent a way as possible.

1.1 Extensions of the SM analysis

The production rates of Higgs-like signals in various decay channels may be modified with respect to the SM prediction in some Higgs doublet models (2HDM) [10]. States which share decay modes and are comparable in mass are strongly motivated in multi-Higgs sectors. For example, within a 2HDM, the CP-even h, H and the CP-odd A may all share a diphoton final state. Depending on the admixture, the relative rates of two states decaying into a diphoton final state can be comparable. Near mass degeneracy and larger mass splitting are predicted in some of these models. Searching for a pair of Higgs bosons within the current analysis range can be a test of these theories.

Deviations of the production rate from the SM expectation could be due to the presence of a second, nearly mass-degenerate Higgs boson [11–13]. If the mass difference between the two signals is of the order of the experimental resolution or smaller, then the apparent width of the observed boson can be enlarged. Furthermore, non SM decays of the Higgs can manifest themselves as a broadening of the width of the observed particle with respect to the SM expectation. The SM Higgs, with m_{H}=125 GeV, has a natural width of 4 MeV which is considerably less than our detector resolution (of order 1 GeV may be achievable for the very best photons) so a measurement of the width for a SM Higgs is unfeasable.

It is therefore relevant to quantify the sensitivity of the Higgs search to a second boson, either very close in mass or more generally anywhere in the mass range of the analysis, and set an upper limit on the width of the observed state.

1.2 Spin

The Landau-Yang theorem forbids the direct decay of a spin-1 particle into a pair of photons [14, 15]. Consequently the spin analysis compares the expectation of the spin-0 SM Higgs, 0^+, and the spin-2 *graviton-like* model with minimal couplings, 2^+_m, [16]. The 2^+_m graviton reso-

nance is produced in one of two ways, gluon-fusion (gg) or quark-antiquark annihilation ($q\bar{q}$). We present hypothesis tests between the 0^+ and the 2^+_m varying the the amount of 2^+_m production from $q\bar{q}$. For the 0^+ SM resonance all production modes have been considered; gluon-fusion, vector-boson-fusion, W and Z boson associated production and top-antitop associated production.

As the 2^+_m is just one of many spin-2 models we have attempted to make the analysis as model independent as possible. As a means of discriminating the two hypotheses we use the scattering angle in the Collins-Sopper frame, $\cos(\theta^*_{\mathrm{CS}})$ [17], which is defined as the angle, in the diphoton rest frame, between the collinear diphotons and the line which bisects one incoming beam with the negative of the other beam,

$$\cos(\theta^*_{\mathrm{CS}}) = 2 \times \frac{E_2 p_{z1} - E_1 p_{z2}}{m_{\gamma\gamma}\sqrt{m^2_{\gamma\gamma} + p^2_{T\gamma\gamma}}}, \tag{1}$$

where E_1 and E_2 are the energies of the leading and trailing photon, p_{z1} and p_{z2} are the z-component momenta of the leading and trailing photon and $m_{\gamma\gamma}$ and $p_{T\gamma\gamma}$ are the invariant mass and transerve momenta of the diphoton system.

In its rest frame the photons from the decay of a spin-0 boson are isotropic. Hence prior to acceptance cuts, the distribution of $\cos(\theta^*_{\mathrm{CS}})$ under the 0^+ hypothesis is uniformly flat. In general this is not the case for spin-2 decays.

2 The CMS detector

A detailed description of the CMS detector can be found elsewhere [18]. The central feature is a superconducting solenoid, 13 m in length and 6 m in diameter, which provides an axial magnetic field of 3.8 T. The bore of the solenoid is instrumented with particle detection systems. The steel return yoke outside the solenoid is instrumented with gas detectors used to identify muons. Charged particle trajectories are measured by the silicon pixel and strip tracker, with full azimuthal coverage within $|\eta| < 2.5$, where the pseudorapidity η is defined as $\eta = -\ln[\tan(\theta/2)]$, with θ being the polar angle of the trajectory of the particle with respect to the counterclockwise beam direction. A lead-tungstate crystal electromagnetic calorimeter (ECAL) and a brass/scintillator hadron calorimeter (HCAL) surround the tracking volume and cover the region $|\eta| < 3$. The ECAL barrel extends to $|\eta| < 1.479$ while the ECAL endcaps covers the region $1.479 < |\eta| < 3.0$ A lead/silicon-strip preshower detector is located in front of the ECAL endcap in the region $1.653 < |\eta| < 2.6$. The preshower detector includes two planes of silicon sensors measuring the x and y coordinates of the impinging particles. A steel/quartz-fibre Čerenkov forward calorimeter extends the calorimetric coverage to $|\eta| < 5.0$. In the region $|\eta| < 1.74$, the HCAL cells have widths of 0.087 in both pseudorapidity and azimuth (ϕ). In the (η, ϕ) plane, and for $|\eta| < 1.48$, the HCAL cells map on to 5×5 ECAL crystal arrays to form calorimeter towers projecting radially outwards from points slightly offset from the nominal interaction point. In the endcap, the ECAL arrays matching the HCAL cells contain fewer crystals. Calibration of the ECAL uses $\pi^0 \to \gamma\gamma$, $\mathrm{W} \to e\nu$, and $\mathrm{Z} \to e^+e^-$ decays. Deterioration of transparency of the ECAL crystals due to irradiation during the LHC running periods and their subsequent recovery is monitored continuously and corrected for using light injected from a laser and LED system [19].

3 Data samples

The dataset consists of events collected with diphoton triggers and corresponds to an integrated luminosity of 5.1 fb^{-1} (19.6 fb^{-1}) at 7 TeV (8 TeV). The spin analysis is carried out on the 8 TeV dataset alone. Diphoton triggers with asymmetric transverse energy (E_{T}) thresholds and complementary photon selections are used. One selection requires a loose calorimetric identification based on the shape of the electromagnetic shower and loose isolation requirements on the photon candidates, while the other requires only that the photon candidate has a high value of the R_9 shower shape variable.[1] The E_{T} thresholds at trigger level are 26(18) GeV and 36(22) GeV on the leading(trailing) photon depending on the running period.

As the instantaneous luminosity delivered by the LHC has increased, it ha become necessary to tighten the isolation requirement applied in the trigger. In order to maintain high trigger efficiency, all four combinations of threshold and selection criteria were deployed (i.e. with both photon candidates fulfilling the R_9 condition, with the high threshold candidate fulfilling the R_9 condition and the low threshold candidate fulfilling the loose ID and isolation, and so on). Accepting events that satisfy any of these triggers results in a trigger efficiency greater than 99% for events passing the offline selection. The total trigger efficiency was found to be uniform in the analysed datasets. Samples of Monte Carlo (MC) events, used for the multi-variate analysis (MVA) trainings and to describe the signal, are fully simulated using GEANT4 [20]. The simulated events include the effects of pile-up, and they are reweighted to reproduce the expected distribution of the number of interactions taking place in each bunch crossing.

4 Photon reconstruction and identification

Photon candidates are reconstructed from the energy deposits in the ECAL, grouping its channels into a supercluster. The superclustering algorithms achieve an almost complete collection of the energy of photons (and electrons) that convert into electron-positron pairs (emit bremstrahlung) in the material in front of the ECAL. In the barrel region, superclusters are formed from five-crystal-wide strips in η, centred on the locally most energetic crystal (seed), and have a variable extension in ϕ. In the endcaps, where the crystals are arranged according to an x-y rather than an η-ϕ geometry, matrices of 5×5 crystals (which may partially overlap) around the most energetic crystals are merged if they lie within a narrow ϕ road. The photon candidates are collected within the ECAL fiducial region $|\eta| < 2.5$, excluding the barrel-endcap transition region $1.4442 < |\eta| < 1.566$. The fiducial region requirement is applied to the supercluster position (defined as the barycentre of the supercluster's active channels) in the ECAL, and a p_{T} threshold is applied after the vertex assignment (see section 5). The exclusion of the barrel-endcap transition region ensures complete containment of the accepted showers in either the ECAL barrel or endcaps .
About half of the photons convert in the material upstream of the ECAL. Conversion track pairs are reconstructed from a combination of Gaussian-sum-filter (GSF) electron tracks and ECAL-seeded tracks fit to a common vertex and then matched to the photon candidate.

4.1 Photon energy

The photon energy is computed starting from the raw crystal energies recorded by the ECAL. In the region covered by the preshower detector ($|\eta| > 1.65$) the energy recorded in that de-

[1] The R_9 variable is defined as the the ratio of the 5x5 crystal energy centred around the seed crystal to the raw supercluster energy. Unconverted photons, having a narrow shower shape will tend to have high values of R_9, while converted photons, with wide shower shapes will tend to have lower values.

tector is added. In order to obtain the best energy resolution, the signals from the crystals are calibrated to compensate several detector effects [19]. The variation of crystal transparency during the run is continuously monitored and corrected for using a correction factor based on the change in response to the light from the laser system. The single-channel response of the ECAL is equalized exploiting the ϕ-symmetry of the energy flow, the mass constraint on the energy of the two photons in π^0/η decays, and the momentum constraint on the energy of isolated electrons from W and Z boson decays. Finally, the containment of the shower in the clustered crystals, and the shower losses for photons which convert in the material upstream of the calorimeter are corrected using a multivariate regression technique based on a Boosted Decision Tree (BDT) [21]. The regression is trained on photons in a sample of simulated events using the ratio of the true photon energy to the raw energy as the target variable. Among the regression input variables are the global η and ϕ coordinates of the supercluster, and a collection of shower shape variables: R_9 of the supercluster, defined previously, the energy weighted η-width and ϕ-width of the supercluster and the ratio of hadronic energy behind the supercluster to the electromagnetic energy of the cluster. In the endcap, the ratio of preshower energy to raw supercluster energy is additionally included. Finally the number of primary vertices and median energy density ρ in the event are included in order to correct residual energy scale effects from pileup. A second BDT provides an event-by-event estimate of the energy uncertainty. It is trained on an independent sample of MC photons. It uses the same input variables as the first BDT but its target is the absolute deviation between the correction predicted by the first regression and the true correction to generator-level energy. The absolute energy scale and the residual long term drifts in the response are corrected using $\mathrm{Z} \to e^+e^-$ decays. The photon energy resolution predicted by the MC simulation is corrected through the addition of a constant gaussian (smearing) term determined from the comparison of the $Z \to e^+e^-$ line-shape in data and MC. The smearing term is extracted differentially as a function of the electrons η and R_9 and by run period.

4.2 Photon identification

The dominant backgrounds to $\mathrm{H} \to \gamma\gamma$ arise from QCD processes and consist of an irreducible fraction from prompt diphoton production, and a reducible one from $pp \to \gamma + \text{jet}$ and $pp \to \text{jet} + \text{jet}$ processes, where one or more of the objects reconstructed as a photon correspond to a jet. Typically these jets contain a neutral meson taking a substantial fraction of the total jet p_T and so appearing as isolated. At large transverse momenta, the photons from the neutral meson decays are collimated and are reconstructed as a single photon in the ECAL. These reconstructed objects are generally referred to as *fake* photons.

The photons entering the analysis need to satisfy some preselection criteria. These consist of an electron veto (removing the candidate photon if its supercluster is matched to a GSF-electron with hits on the innermost tracker layer and it is not not matched to a reconstructed conversion), a selection on the hadronic leakage of the shower (measured as the ratio of the hadronic energy in the HCAL towers behind the supercluster to the ECAL energy in the supercluster) and a loose selection based on isolation and on the shape of the shower. Additionally photons are required to have, $p_T/m_{\gamma\gamma} > 1/3$ ($p_T/m_{\gamma\gamma} > 1/4$) for the leading (subleading) photon and $|\eta_{\text{cluster}}| < 2.5$ for all photons, where p_T is the transverse momentum of a photon, $m_{\gamma\gamma}$ is the diphoton invariant mass and $|\eta_{\text{cluster}}|$ is the pseudorapidity of the photon supercluster. In addition photons are rejected whose supercluster lies within the barrel-endcap transition region, $1.4442 < |\eta_{\text{cluster}}| < 1.566$.

The preselection criteria were optimized to emulate the trigger and to reject electrons. The efficiency of the photon preselection is measured in data using the "tag and probe" technique [22].

The efficiency of all preselection criteria except the electron veto requirement is determined using $Z \to e^+e^-$ events. The efficiency for photons to satisfy the electron veto is measured using $Z \to \mu^+\mu^-\gamma$ events, where the photon is produced by final-state radiation. This provides a more than 99% pure source of prompt photons. The efficiency of the preselection criteria is calculated in four photon categories which depened upon the η and R_9 of the photon. For events with a Higgs boson of 125 GeV, the efficiency ranges from 92% to 99% and the ratio $\epsilon_{data}/\epsilon_{MC}$ is consistent with 1 within uncertainties in all categories. The measured $\epsilon_{data}/\epsilon_{MC}$ ratios are used to correct the simulated signal sample and the associated uncertainties are taken into account in the signal extraction procedure.

The SM extension measurements (natural width and second Higgs scenarios) use the MVA-based photon selection described in Ref. [9]. The spin analysis uses the cut-based photon selection described in Ref. [9] in order to reduce model dependence.

5 Diphoton vertex

The mean number of pp interactions per bunch crossing is 9.5 (19.9) in the 7 TeV (8 TeV) dataset with a corresponding variance of 4.8(7.3). The interaction vertices are built using the reconstructed tracks from the produced charged particles. Their distribution in the longitudinal direction (z), has an RMS spread of about 6 cm (5 cm) in the 7 TeV (8 TeV) dataset.

The diphoton mass resolution is driven by the photon energy resolution and the determination of the direction of the photons, which is dominated by the knowledge of the vertex from which they originate. The relative contribution from the vertex assignment to the mass resolution becomes negligible with respect to the photon energy resolution when the distance between the chosen vertex and the true one is below 1 cm.

Since photons are neutral particles, and therefore do not leave an ionization signal in the tracker, the diphoton vertex is identified indirectly. The vertex can be identified using the kinematic properties of the diphoton system and their correlations with the kinematic properties of the recoiling tracks. If either of the photons converts, the direction of the converted photon tracks and the conversion position can be used to identify the diphoton interaction vertex.

Details of how we determine the diphoton vertex and estimate the per-event vertex probability are given in Ref. [9].

6 Systematic uncertainties

The systematic uncertainties affecting the signal model are for the most part identical to those detailed in the SM analysis [9]. Most of the uncertainties are common to all the analyses. They enter the likelihood as nuisance parameters which allow the shape and normalisation of the signal model to be modified. The systematic uncertainties are summarised in Table 1.

The systematic uncertainties calculated at the single photon level are:

- *Photon selection efficiency:* taken to be the largest uncertainty associated with the data/MC scale factors separately for the ECAL barrel and endcap.
- *Energy scale and resolution:* scale and resolutions are studied with electrons from $Z \to e^+e^-$ and then applied to photons. The main source of systematic uncertainty is the different interactions of electrons and photons with matter. Uncertainties are assessed by changing the rescaling of the R_9 distributions, changing the R_9 selection,

the regression training and the electron selection used.

- *Photon identification:* taken as the largest uncertainty on the data/MC scale factors computed on $Z \to e^+e^-$ events using a tag-and-probe technique. This systematic uncertainty is applied to the photon identification in the cut-based spin analysis and to the loose photon preselection in the MVA SM extensions analyses.
- *R_9 selection (spin analysis only):* taken from the data/MC comparison of the photon R_9 categorization in $Z \to \mu\mu\gamma$ events. The statistical uncertainty on the single photon is propagated to the diphoton categories and the result is assigned as a systematic uncertainty on the category migration between low and high R_9 categories.
- *Photon identification BDT and photon energy resolution BDT (SM extensions analyses only):* the agreement between data and simulation is assessed using $\mathrm{Z} \to e^+e^-$ candidates, $\mathrm{Z} \to \mu^+\mu^-\gamma$ candidates and the highest transverse energy photon in the diphoton invariant mass region where $m_{\gamma\gamma} > 160\,\mathrm{GeV}$ (the fake photon contribution becomes smaller at high diphoton invariant mass). Both the inputs to the diphoton BDT and its output value are compared. A variation of ± 0.01 on the photon identification BDT output value, together with an uncertainty on the per-photon energy resolution estimate, parametrized as a rescaling of the resolution estimate by $\pm 10\%$ about its nominal value, fully covers the differences observed between data and MC simulation.

The systematic uncertainties calculated at the event level are:

- *Integrated luminosity:* the luminosity uncertainty is estimated as described in Ref. [23].
- *Vertex finding efficiency:* taken from the statistical uncertainty on the data/MC scale factor on $Z \to \mu^+\mu^-$ and the uncertainty on the signal p_T distribution arising from the theoretical uncertainties.
- *Trigger efficiency:* the systematic uncertainties are extracted from $Z \to e^+e^-$ using a tag-and-probe technique and rescaling them to take into account the different R_9 distributions for electrons and photons.
- *Higgs p_T spectrum (Spin analysis only):* this is introduced to account for potential differences between the data and MC distributions of the Higgs transverse momenta, p_T, which can distort the shape of the $\cos(\theta^*_{\mathrm{CS}})$ distribution. The uncertainties are implemented as the category migrations which result from shifting the Higgs p_T spectrum by 10%

The theoretical systematic uncertainties considered are:

- *Production cross section:* the systematic uncertainties on the production cross section follow the recommendation of the LHC Higgs cross section working group [24]
- *Scale and PDF uncertainties (SM extensions analyses only):* in addition, to account for signal event migration between classes due to PDF uncertainties, the uncertainty on the signal cross section has been determined using the PDF4LHC prescription [25–29]. The uncertainty on the relative event class yields due to the scale uncertainty has been estimated by varying the renormalization and factorization scales used by MC@NLO [30] and MCFM [31], between $m_\mathrm{H}/2$ and $2 \times m_\mathrm{H}$, and examining the effect on the Higgs boson kinematic properties in terms of rapidity and transverse momentum. By deriving weights defined as the ratio of the differential cross section in the varied case to that in the nominal, the effect on the event class yields can be determined. This effect is a migration of signal events between classes, which can be as large as 12.5% (these uncertainties are not listed in Table 1). The effect of

PDF uncertainties on the relative event class yields has been determined in a similar fashion, by varying the Higgs boson kinematic properties according to the variations of the 26 eigenvalues of the CT10 [32] PDF set within their uncertainties. The largest migration of signal events between classes due to the PDF uncertainties is 1.3%.

Table 1: Separate sources of systematic uncertainties accounted for in the analysis of the 8 TeV data set.

Sources of systematic uncertainty		**Uncertainty**	
Per photon		Barrel	Endcap
Energy resolution ($\Delta\sigma/E_{MC}$)	$R_9 > 0.94$ (low η, high η)	0.23%, 0.72%	0.93%, 0.36%
	$R_9 < 0.94$ (low η, high η)	0.25%, 0.60%	0.33%, 0.54%
Energy scale ($(E_{data} - E_{MC})/E_{MC}$)	$R_9 > 0.94$ (low η, high η)	0.20%, 0.71%	0.88%, 0.12%
	$R_9 < 0.94$ (low η, high η)	0.20%, 0.51%	0.18%, 0.12%
Photon identification efficiency		1.0%	2.6%
Spin analysis only:			
$R_9 >$ 0.94 efficiency (results in class migration)		4.0%	6.5%
SM extension analyses only:			
Photon identification BDT		$\pm$0.01 (shape shift)	
(Effect of up to 4.3% event class migration.)			
Photon energy resolution BDT		$\pm$10% (shape scaling)	
(Effect of up to 8.1% event class migration.)			
Per event			
Integrated luminosity		4.4%	
Vertex finding efficiency		0.2%	
Trigger efficiency		1.0%	
Global energy scale		0.47%	
Spin analysis only:			
Higgs p_T uncertainty		10%	
Production cross sections		Scale	PDF
Gluon fusion		+7.6% -8.2%	+7.6% -7.0%
Vector boson fusion		+0.3% -0.8%	+2.6% -2.8%
Associated production with W/Z		+2.1% -1.8%	4.2%
Associated production with $t\bar{t}$		+4.1% -9.4%	8.0%

7 Reinterpreting the data with new parameters

The following section presents results on extensions to the SM analysis which, by including additional terms in the likelihood estimator, allow further measurements to be made. The following preliminaries to the analysis follow the exact prescription described in the SM search in Ref. [9],

- Event categorisation
- Background Model
- Systematic Uncertainties
- Signal Model

7.1 Decay width

To accomodate the natural width of the Higgs boson, the Gaussian components used in the signal model of the SM analysis, where the signal width is assumed to be neglible as compared to the detector resolution, are replaced by an analytic convolution of a Breit-Wigner distribution (modelling a non-zero decay width) with a Gaussian distribution (modelling the non-zero detector resolution).

A profile likelihood estimator is used to calculate upper limits on the width of the observed boson whilst allowing the fitted Higgs mass to float. Figure 1 shows a scan of the negative-log-likelihood as a function of the observed state's decay width for the combined 7 and 8 TeV dataset. The observed (expected) upper limit on the width is calculated using the Feldman-Cousins method [33] and is found to be 6.9 (5.9) GeV at 95% confidence level.

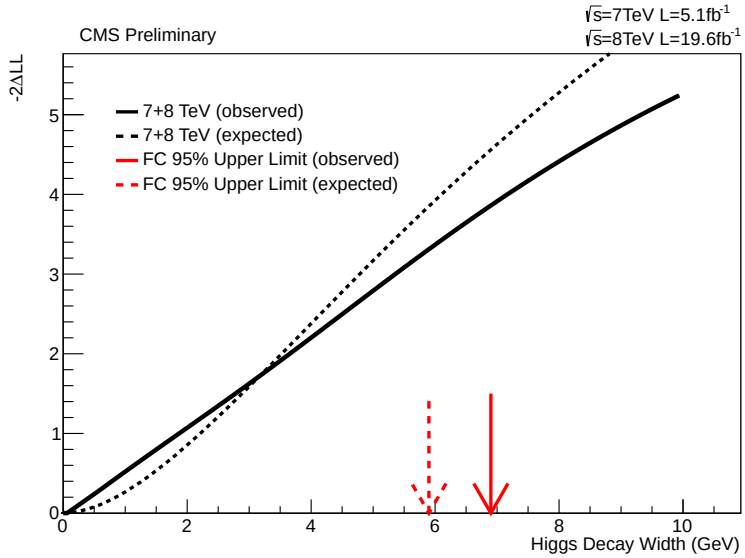

Figure 1: A scan of the negative-log-likelihood as a function of the Higgs decay width. The observed (expected) Feldman-Cousins upper limit on the width is 6.9 (5.9) GeV at 95% confidence level.

7.2 Search for additional Higgs-like states

In this search the observed state around 125 GeV is considered as part of the background. The background model now becomes the SM analysis signal plus background model, such that the mass and signal strength of the already observed state are allowed to float. An additional independent signal model is introduced as a second Higgs for which exclusion limits on the signal strength, and associated p-value, can be calculated. The resulting exclusion limit is shown in Fig. 2. Once sufficiently away from 125 GeV, we recover the same limit as in the search for a single SM Higgs boson. The p-value at the most significant excess, where m_{H}=136.5 GeV, is found to be 2.93σ. The shaded area, of 125$\pm$3 GeV, indicates the region where the expected sensitivity to a second Higgs boson is degraded due to the presence of the already observed state. This region is probed by the search described in Section 7.3.

Additional cases of interest are when the second state couples only to fermions or only to bosons, for example in the alignment limit of some 2HDM scenarios. The alignment limit, defined as $\sin^2(\beta - \alpha) = 1$, where α and β are the two mixing angles in 2HDMs, h has SM couplings and H and A decouple from the W and Z bosons, therefore gluon-fusion is the

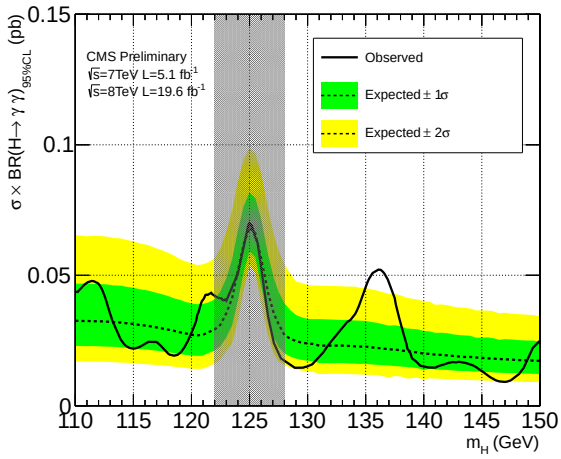

Figure 2: Exclusion limit on $\sigma \times BR$ for another Higgs state with SM couplings taking the observed state at 125 GeV as part of the background

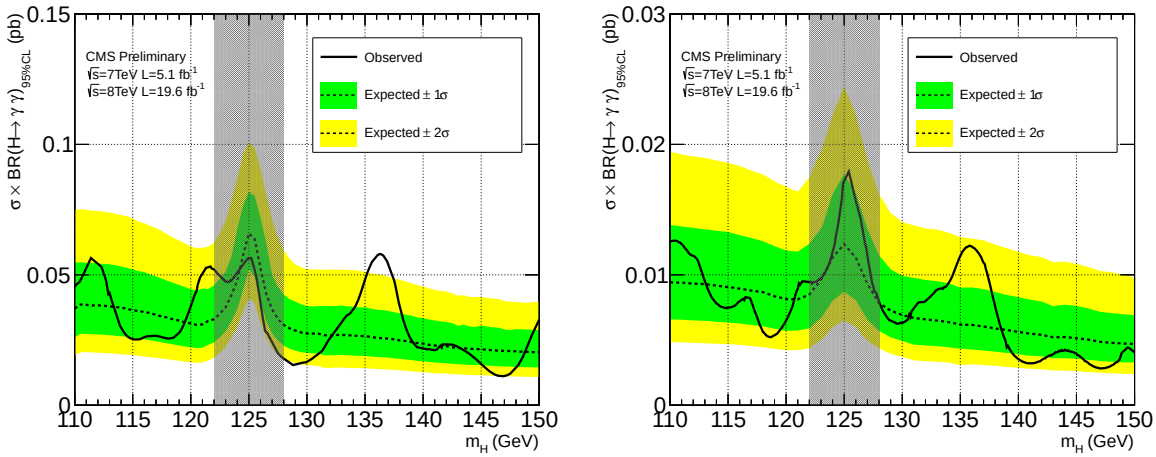

Figure 3: Exclusion limits on $\sigma \times BR$ for a second Higgs-like state produced with gluon-fusion only (left) or vector-boson-fusion and vector-boson-associated production only (right) taking the observed state at 125 GeV as part of the background.

only relevant production mechanism. We assume that the state near 125 GeV has SM couplings, with floating mass and signal strength, and search for additional states with only gluon-fusion production (Fig. 3a) and only vector-boson-fusion and vector-boson-associated production (Fig. 3b). The local p-value at the most significant excess, which in both cases is where m_{H}=136.5 GeV, is found to be 2.73σ for gluon-fusion production only and 2.15σ for vector-boson production only.

7.3 Search for two near mass-degenerate states

Because of the high resolution of the diphoton channel, there is some sensitivity to a pair of nearby states. The analysis uses the one-Higgs search event selections but the signal model is re-parameterized such that two mass variables, m_{H} and $m_{\mathrm{H2}} = m_{\mathrm{H}} + \Delta m$, refer to two similar but independent signals. The relative strength of the two signals, parametrised by the variable x, is allowed to float such that the two signals are modulated by rx and $r(1-x)$ respectively,

where r is the total signal strength and x is the fraction of signal contained in the state lower in mass. A 2D scan of Δm and x is obtained by profiling over m_{H} and r, shown in Fig. 4 for the expecation (left) and observation (right). We expect to be sensitive in regions where Δm is close to or greater than the experimental mass resolution and where both signal strengths are significant. The data disfavours at 95% C.L. cases for which the signal lower in mass is around 4 times the strength of the signal higher in mass, where the signals are separated by greater than 4 GeV.

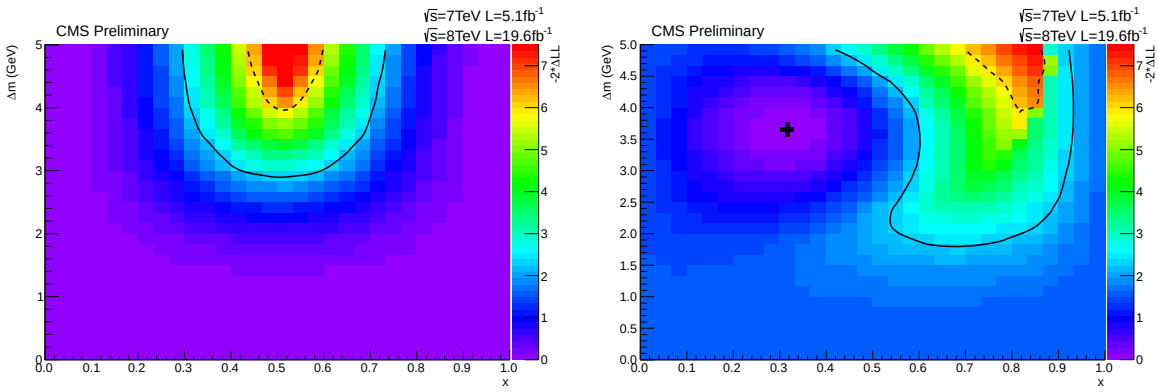

Figure 4: A 2D negative-log-likelihood scan for two near mass-degenerate states parametrised by Δm (the mass difference between the states) and x (the fraction of signal in the lower mass state). The black cross shows the best fit value, the solid and dashed lines correspond to the 68% and 95% confidence level contours respectively for the expectation (left) and observation (right).

8 Spin hypothesis separation

8.1 Event categorisation

The effect of the photon selection cuts on the distributions of $|\cos(\theta^*_{\mathrm{CS}})|$ is illustrated in Fig. 5. Before any acceptance cuts, Fig. 5 (left), the $|\cos(\theta^*_{\mathrm{CS}})|$ distribution of the 0^+ processes is flat. This is not the case for the 2^+_m processes (gluon-fusion and quark-antiquark annihilation). After the selection cuts are applied these distributions are considerably distorted, Fig. 5 (right). As a Higgs produced from vector-boson-fusion, which is ∼8% of the total (compared to ∼88% from gluon fusion), is typically produced at higher transverse momentum there is some additional contribution of 0^+ signal at high values of $|\cos(\theta^*_{\mathrm{CS}})|$ compared to the 2^+_m production modes after the selection cuts.

A robust analysis is possible because although the acceptance × efficiency varies considerably as a function of $|\cos(\theta^*_{\mathrm{CS}})|$, the shape of this variation is largely independent of the spin-parity model. This is also true in restricted ranges of η and R_9 which allows us to extract the signal yield in bins of $|\cos(\theta^*_{\mathrm{CS}})|$ in a comparatively model independent way. Figure 6 shows the efficiency × acceptance ratio between the 2^+_m (with gluon-fusion production only) and 0^+ (all SM production modes) as a function of $|\cos(\theta^*_{\mathrm{CS}})|$ in the $|\eta|$ and R_9 categories defined in Table 2. It is clear that the acceptance × efficiency between the spin-0 and spin-2 models is independent of $|\cos(\theta^*_{\mathrm{CS}})|$ apart from at high values of $|\cos(\theta^*_{\mathrm{CS}})|$ where the vector-boson-fusion production in the SM plays a role. This motivates the choice of $|\cos(\theta^*_{\mathrm{CS}})|$ category boundaries described below where all the categories have similar efficiency × acceptance apart from the bin highest in $|\cos(\theta^*_{\mathrm{CS}})|$.

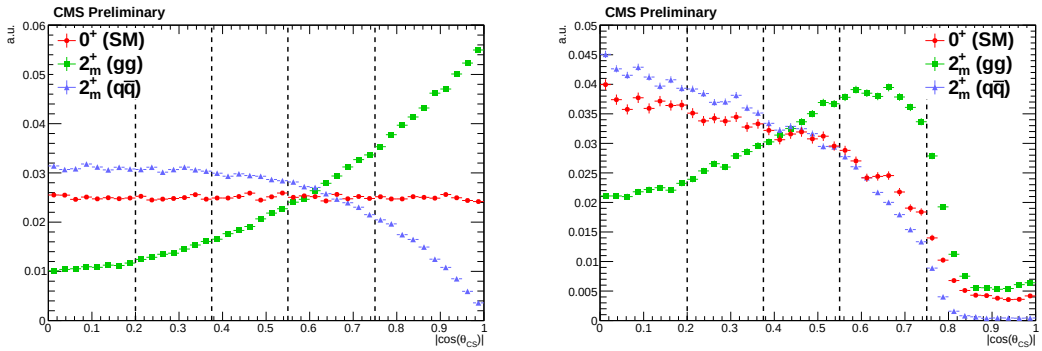

Figure 5: The distribution of $|\cos(\theta^*_{\mathrm{CS}})|$ before any selection cuts (left) and after the selection cuts (right). The three histograms represent the spin 0^+ distribution with all SM production modes (red circular points), the spin 2^+_m distribution with the gluon-fusion production mode (green square points) and the spin 2^+_m distribution with the quark-antiquark annihilation production mode (blue triangular points). The $|\cos(\theta^*_{\mathrm{CS}})|$ category boundaries are shown as the black dashed lines.

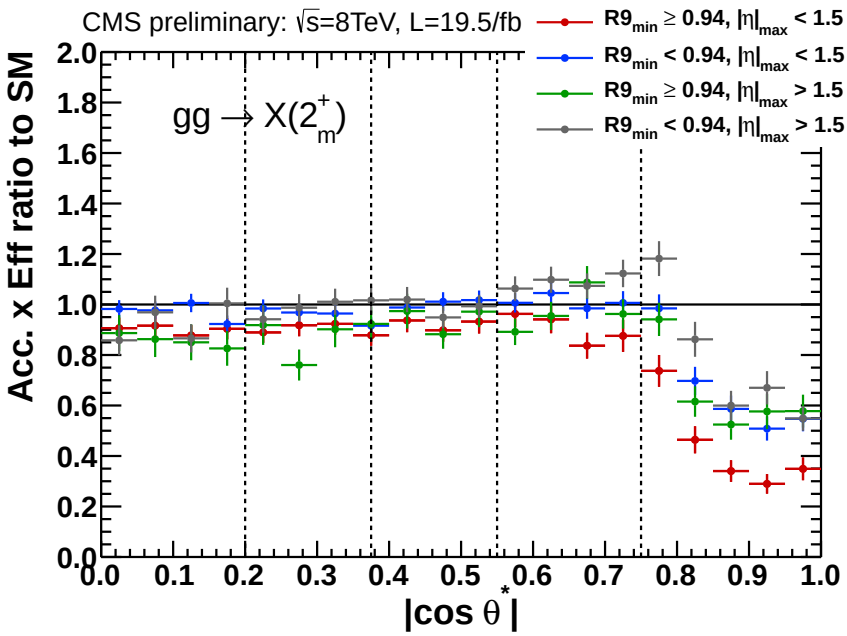

Figure 6: Acceptance $\times$ efficiency ratio between the 2^+_m (gluon-fusion production) and 0^+ (all SM production modes) of the event selection as a function of $|\cos(\theta^*_{\mathrm{CS}})|$ split into the $|\eta|$ and R_9 categories defined in Table. 2. The $|\cos(\theta^*_{\mathrm{CS}})|$ category boundaries are shown as the black dashed lines.

Category 0	$\lvert\eta\rvert_{\max} < 1.5$	and	$R_{9_{\min}} > 0.94$
Category 1	$\lvert\eta\rvert_{\max} < 1.5$	and	$R_{9_{\min}} \leq 0.94$
Category 2	$\lvert\eta\rvert_{\max} > 1.5$	and	$R_{9_{\min}} > 0.94$
Category 3	$\lvert\eta\rvert_{\max} > 1.5$	and	$R_{9_{\min}} \leq 0.94$

Table 2: Definition of photon resolution categories

Spin Category 0		$\lvert\cos(\theta^*_{\mathrm{CS}})\rvert < 0.2$
Spin Category 1	$0.2 \leq$	$\lvert\cos(\theta^*_{\mathrm{CS}})\rvert < 0.375$
Spin Category 2	$0.375 \leq$	$\lvert\cos(\theta^*_{\mathrm{CS}})\rvert < 0.55$
Spin Category 3	$0.55 \leq$	$\lvert\cos(\theta^*_{\mathrm{CS}})\rvert < 0.75$
Spin Category 4	$0.75 \leq$	$\lvert\cos(\theta^*_{\mathrm{CS}})\rvert < 1.0$

Table 3: Definition of photon $\lvert\cos(\theta^*_{\mathrm{CS}})\rvert$ categories

To benefit from the improved energy resolution of non-showering photons in the barrel, each event is categorised in η and R_9 according to Table 2.

Within each category events are binned in $\lvert\cos(\theta^*_{\mathrm{CS}})\rvert$, to discrimate between the different spin hypotheses, according to Table. 3.

The $\lvert\cos(\theta^*_{\mathrm{CS}})\rvert$ boundaries are optimised to make particular use of the most disciminating bin (high $\lvert\cos(\theta^*_{\mathrm{CS}})\rvert$) and to maintain uniform acceptance $\times$ efficiency in the other bins. In total the analysis is split into 20 event classes (4 η/R_9 categories $\times$ 5 $\lvert\cos(\theta^*_{\mathrm{CS}})\rvert$ categories).

8.2 Signal models

The signal models are obtained from MC simulation and enter the likelihood as binned histograms with a bin width of 0.5 GeV. For the spin-0 SM processes (ggH, qqH, VH, ttH) the simulation uses the next-to-leading order (NLO) matrix-element generator POWHEG [34, 35] interfaced with PYTHIA [36]. For the dominant gluon fusion process POWHEG has been tuned following the recommendations of the LHC Higgs Cross Section Working Group [37] to reproduce the HQT (NNLO+NNLL) spectrum. For the spin-2 *graviton-like* processes (gg, $q\bar{q}$) the simulation uses the JHU generator at leading-order interfaced with PYTHIA [16]. The results were also cross checked using spin-0 MC with the JHU generator. All samples are run through the full CMS simulation using GEANT4 [20]. The MC is generated at m_{H}=125 GeV and m_{H}=126 GeV, the signal model histograms are linearly interpolated when evaluating for any intermediate value of m_{H}. Systematic uncertainties enter the likelihood as binned templates representing shifts of $\pm 1\sigma$ for each systematic under consideration. More details of the specific systematic uncertainties applied are outlined in Sec. 6.

The expected signal yield for the *graviton-like* samples after the selection cuts is normalised such that when no $\cos(\theta^*_{\mathrm{CS}})$ discrimination is used both the spin-0 and spin-2 models extract the same number of signal events. Table 4 shows the expected number of signal events, the effective width (half the narrowest range which contains 68.3% of the distribution), σ_{eff}, and the full width at half the maximum (divided by 2.35), FWHM/2.35, at m_{H}=125 GeV, for the 0^+ and 2^+_m production processes, the estimated number of background events and the observed number of events, at $m_{\gamma\gamma}$ =125 GeV, in each category.

Expected signal and estimated background

Event classes		Expected signal (m_H=125 GeV) $pp \to 0^+$ Ev. % total	σ_{eff} (GeV)	FWHM / 2.35 (GeV)	$gg \to 2^+_m$ Ev. % total	σ_{eff} (GeV)	FWHM / 2.35 (GeV)	$q\bar{q} \to 2^+_m$ Ev. % total	σ_{eff} (GeV)	FWHM / 2.35 (GeV)	Background $m_{\gamma\gamma} = 125$ GeV (Ev./GeV)	Data $m_{\gamma\gamma} = 125$ GeV (Ev./GeV)
$\lvert\eta\rvert < 1.44$, $R_9 > 0.94$	$\lvert\cos(\theta^*_{CS})\rvert < 0.2$	10.50	1.66	1.46	6.10	1.59	1.34	9.21	1.87	1.49	109.4 $\pm$ 1.1	115
	$0.2 \leq \lvert\cos(\theta^*_{CS})\rvert < 0.375$	7.78	1.62	1.38	6.06	1.62	1.40	6.82	1.85	1.53	91.7 $\pm$ 1.0	96
	$0.375 \leq \lvert\cos(\theta^*_{CS})\rvert < 0.55$	5.94	1.59	1.42	6.38	1.61	1.47	4.93	1.72	1.47	83.1 $\pm$ 0.9	101
	$0.55 \leq \lvert\cos(\theta^*_{CS})\rvert < 0.75$	3.78	1.63	1.54	5.99	1.56	1.45	2.67	1.70	1.61	77.1 $\pm$ 0.9	88
	$0.75 \leq \lvert\cos(\theta^*_{CS})\rvert < 1.0$	1.14	1.51	1.43	1.44	1.48	1.37	0.20	1.69	1.59	16.3 $\pm$ 0.4	19
$\lvert\eta\rvert < 1.44$, $R_9 \leq 0.94$	$\lvert\cos(\theta^*_{CS})\rvert < 0.2$	12.75	2.00	1.68	7.72	2.00	1.72	12.48	2.14	1.81	196.7 $\pm$ 1.5	192
	$0.2 \leq \lvert\cos(\theta^*_{CS})\rvert < 0.375$	9.48	1.96	1.68	7.59	1.94	1.66	9.08	2.11	1.81	163.1 $\pm$ 1.3	204
	$0.375 \leq \lvert\cos(\theta^*_{CS})\rvert < 0.55$	8.00	2.00	1.76	8.63	2.07	1.83	7.05	2.12	1.91	163.3 $\pm$ 1.3	152
	$0.55 \leq \lvert\cos(\theta^*_{CS})\rvert < 0.75$	6.23	2.06	1.84	9.73	2.10	1.83	4.85	2.17	1.87	177.8 $\pm$ 1.4	194
	$0.75 \leq \lvert\cos(\theta^*_{CS})\rvert < 1.0$	1.65	2.12	1.98	2.87	2.22	2.06	0.45	2.35	2.16	46.7 $\pm$ 0.6	49
$\lvert\eta\rvert > 1.44$, $R_9 > 0.94$	$\lvert\cos(\theta^*_{CS})\rvert < 0.2$	3.08	3.55	3.52	1.75	3.51	3.39	6.15	3.64	3.44	74.6 $\pm$ 0.9	66
	$0.2 \leq \lvert\cos(\theta^*_{CS})\rvert < 0.375$	2.38	3.17	3.06	1.87	3.02	2.93	3.87	3.35	3.27	44.7 $\pm$ 0.7	50
	$0.375 \leq \lvert\cos(\theta^*_{CS})\rvert < 0.55$	3.05	3.04	2.96	3.42	3.00	2.87	3.91	3.13	2.92	66.8 $\pm$ 0.8	72
	$0.55 \leq \lvert\cos(\theta^*_{CS})\rvert < 0.75$	4.12	3.09	2.97	6.81	3.09	2.91	4.26	3.16	2.91	131.4 $\pm$ 1.2	132
	$0.75 \leq \lvert\cos(\theta^*_{CS})\rvert < 1.0$	1.62	2.67	2.38	2.87	2.79	2.72	0.55	3.16	3.09	52.1 $\pm$ 0.7	52
$\lvert\eta\rvert > 1.44$, $R_9 \leq 0.94$	$\lvert\cos(\theta^*_{CS})\rvert < 0.2$	3.35	3.37	3.00	1.87	3.52	3.43	5.64	3.57	3.41	107.5 $\pm$ 1.1	87
	$0.2 \leq \lvert\cos(\theta^*_{CS})\rvert < 0.375$	4.10	3.37	3.30	3.19	3.27	3.09	6.17	3.41	3.27	116.2 $\pm$ 1.1	116
	$0.375 \leq \lvert\cos(\theta^*_{CS})\rvert < 0.55$	4.78	3.11	2.90	5.10	3.21	3.11	6.13	3.29	3.18	144.0 $\pm$ 1.2	164
	$0.55 \leq \lvert\cos(\theta^*_{CS})\rvert < 0.75$	4.70	3.14	2.94	7.65	3.16	3.00	4.95	3.21	3.04	221.8 $\pm$ 1.5	209
	$0.75 \leq \lvert\cos(\theta^*_{CS})\rvert < 1.0$	1.58	2.93	2.74	2.94	3.09	3.00	0.57	3.15	3.11	77.4 $\pm$ 0.8	66
	Total	412.5 (Evs.)	2.22	1.77	439.0 (Evs.)	2.28	1.83	491.0 (Evs.)	2.53	1.99	2161.8 $\pm$ 4.8	2224

Table 4: The expected number of 0^+ and 2^+_m signal events (each category's constribution to the total as a percentage), the effective width, σ_{eff}, and the full width at half the maximum divided by 2.35 at m_H=125 GeV, the expected number of background events at $m_{\gamma\gamma}$ =125 GeV and the observed number of events at $m_{\gamma\gamma}$ =125 GeV for each of the 20 event classes.

8.3 Background model

The background model is derived in a similar way to that presented in the SM analysis [9] and is evaluated from the data alone, without reference to MC simulation. The background model is obtained by fitting the diphoton mass spectrum, in each of the event classes, over the range $100 < m_{\gamma\gamma} < 180\,\text{GeV}$. A bias study identical to the one performed in Ref. [9] has been performed to extract a parametrisation of the background model such that any systematic bias incurred by the choice of function is less than 20% of the statistical uncertainty from the fit. Polynomials of order 4 (3) are found to fulfill this criteria for all categories for which $|\cos(\theta^*_{\text{CS}})| < 0.75$ ($0.75 \leq |\cos(\theta^*_{\text{CS}})| < 1.0$).

The $m_{\gamma\gamma}$ distributions, the background fit and its statistical uncertainty, as well as the binned signal model (scaled up by a factor of 5) for the two spin hypotheses, are shown in Figures 10-14 in Appendix A for the 20 different event classes.

8.4 Results

The acceptance $\times$ efficiency of the two spin models in each category as well as the differential cross section as a function of $|\cos(\theta^*_{\text{CS}})|$, which depends only on the spin of the initial state, is obtained from the MC simulation. The only remaining assumption is on the total number of expected signal events for a given spin-parity state and production mode. This is well defined for the spin-0 SM case and is obtained from the $\sigma \times BR$ given by the LHC Higgs cross section working group in Ref. [24]. For the graviton-like 2^+_m this quantity is unknown. Consequently we scale the signal models for both spin hypotheses with a modifier, μ, such that when $\mu = 1$ and all $\cos(\theta^*_{\text{CS}})$ information is ignored, the total number of expected signal events for the model in question is equivalent to the SM expectation. When generating pseduo-experiments for a particular model, the value of all the free parameters in the fit (including the signal nuisance parameters, the background shape parameters and the signal srength μ) are set to their best fit values after fitting the model in question to the data. In this way the expected separation is a fair representation of what we observe in data. All the results described below are evaluated at m_{H}=125 GeV.

8.4.1 SM compabibility check

The signal yield, $\mu = \sigma/\sigma_{SM}$, is extracted independently in each of the $|\cos(\theta^*_{\text{CS}})|$ bins, simultaneously fitting over the η and R_9 bins such that the relative yields in each of the η and R_9 bins is constrained to that predicted by the SM. The result is shown in Figure 7 for the data (black points), the 0^+ model expectation (red line), the 2^+_m model expectation using the gg production mode only (blue line), the 2^+_m model expectation using the $q\bar{q}$ production mode only (green line) and the 2^+_m model expectation using a half-half mixture of gg and $q\bar{q}$ production (magenta line), where for the expectations a single representative toy is used, obtained using asymptotic formulae from Ref. [38], and the normalisation is extracted from a fit to data. The final point of the blue line can be understood by referring back to Figure 6. The fact that the SM ggH and qqH production is of a similar strength at high values of $|\cos(\theta^*_{\text{CS}})|$ causes the fitted strength (when fitting the 0^+ model to the 2^+_m (gg) expectation) to be smaller in the highest $|\cos(\theta^*_{\text{CS}})|$ bin as compared to the second highest, contrary to what might be expected. The χ^2 p-values of the data when fitted with the four hypotheses are shown in Table 5 where the corresponding plots of the best fit to the data of each model in bins of $|\cos(\theta^*_{\text{CS}})|$ are shown in Appendix B.

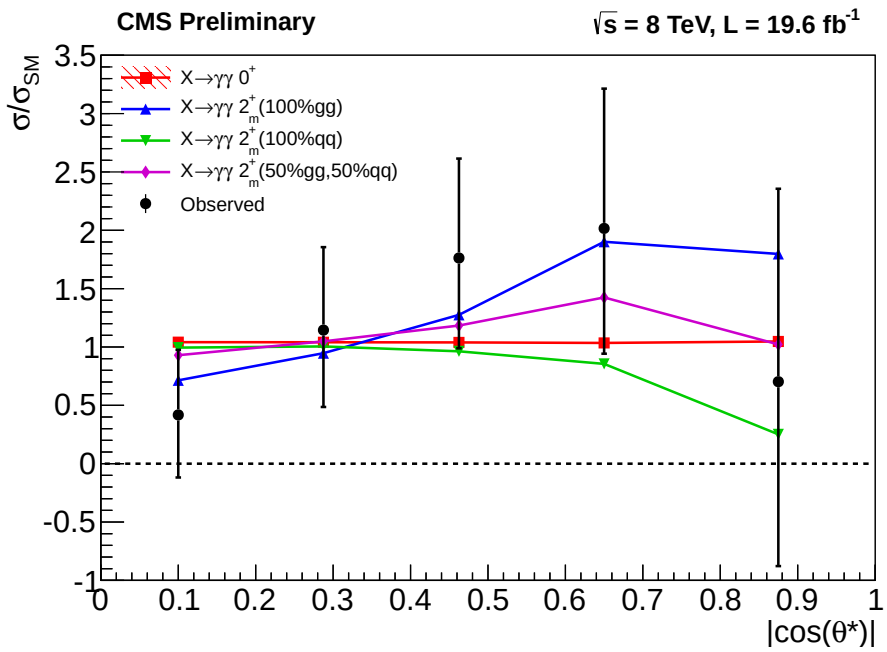

Figure 7: The SM extracted signal yield as a function of $|\cos(\theta^*_{\rm CS})|$ for the 0^+ expectation (red line), 2^+_m expectation with gluon-fusion production only (blue line), the 2^+_m expectation with quark-antiquark annihilation production only (green line), the 2^+_m expectation with half gg, half $q\bar{q}$ production (magenta line) and the observation (black points).

Compatibility	
Source	$\chi^2 p$-value
Data vs. 0^+	0.68
Data vs. 2^+_m (100% gg)	0.91
Data vs. 2^+_m (100% $q\bar{q}$)	0.51
Data vs. 2^+_m (50% gg, 50% qq)	0.81

Table 5: The χ^2 compatibility of the 0^+ and 2^+_m models with the observation.

8.4.2 Hypothesis tests of the SM Higgs, 0^+, vs. graviton-like, 2^+_m

The separation between the two models and the data is extracted using the test statistic defined as twice the negative ratio of the likelihoods for the 0^+ signal plus background hypothesis and the 2^+_m signal plus background hypothesis when performing a simultaneous fit of all twenty event classes together, $q = -2\ln(\mathcal{L}_{2^+_{\rm m}+\rm bkg.}/\mathcal{L}_{0^++\rm bkg.})$.

The distribution of this test statistic is shown in Fig. 8 for pseudoexperiments generated with an overall signal yield which is extracted from a fit to the data for the 0^+ hypothesis (orange) and the 2^+_m hypothesis (blue) for gluon-fusion production only (left) and quark-antiquark annihilation production only (right). The observed value is shown as the red arrow. The $\rm CL_S$ of the observation for the gluon-fusion only spin-2 production is 60.9% whilst for the quark-antiquark production it is 16.9%. Consequently, neither of these spin-2 models can be excluded.

The previous two tests are both performed assuming that the 2^+_m state is produced entirely by either gluon-fusion or quark-antiquark annihilation. A further three points, with mixtures of gg and $q\bar{q}$ spin-2 production, have been tested such that the overall yield of the 2^+_m signal is

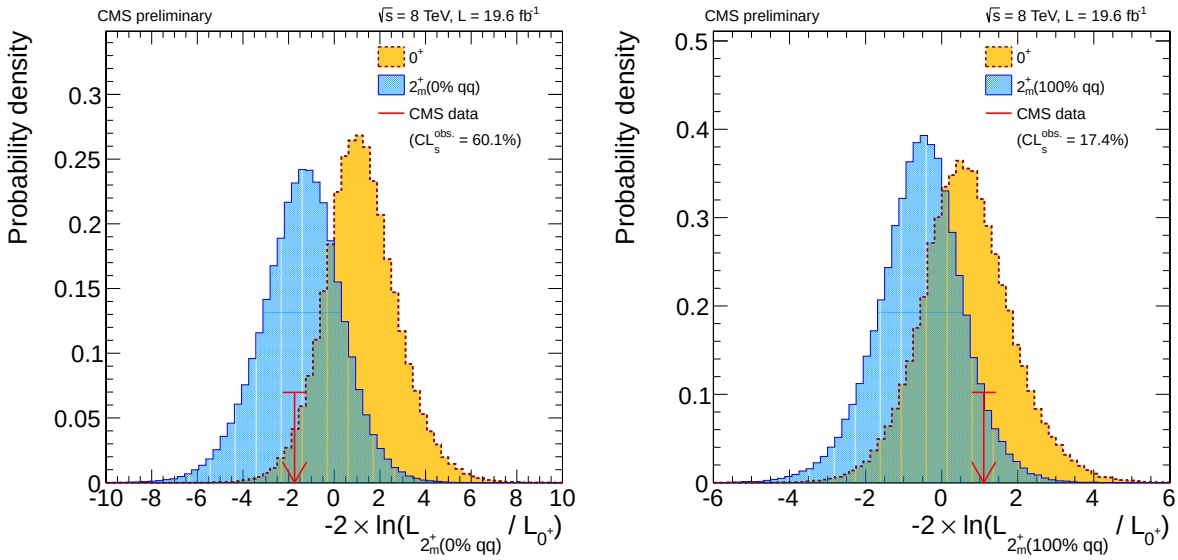

Figure 8: The distribution of the test statistic for pseudo experiments generated under the SM, 0^+, hypothesis (orange) and the *graviton-like*, 2^+_m, hypothesis (blue) with gluon fusion produciton only (left) and quark-antiquark production only (right). The observed value in the data is shown as the red arrow.

fixed to the best fit value of the model in question to data and the fraction of $q\bar{q}$ production is increased by a factor, $f_{q\bar{q}}$. Figure 9 shows the distribution of the test statistic as a function of the fraction of 2^+_m production from $q\bar{q}$ annihilation. Figure 8 is, in effect, a projection of Fig. 9 at the points $f_{q\bar{q}}$ =0% and $f_{q\bar{q}}$ =100% . The test statistic distributions for $f_{q\bar{q}}$ =25%, 50% and 75% are shown in Appendix C.

9 Conclusions

Studies of some of the properties of the observed Higgs-like signal have been performed in the two photon decay channel with 5.1 (19.6) fb^{-1} of pp collisions at a centre-of-mass energy of 7 (8) TeV with the CMS detector. The natural width of the new state is found to be < 6.9 GeV (expected < 5.9 GeV) at 95% C.L. Exclusion limits have been set on second Higgs scenarios either supposing another Higgs elsewhere or that the observed signal is shared between two nearly degenerate mass states. The SM spin-0 hypothesis is compared to a graviton like spin-2 hypothesis with minimal couplings. With the present data this particular spin-2 model cannot be ruled out. The observed data is found to be compatible with the SM with a χ^2 p-value of 0.68.

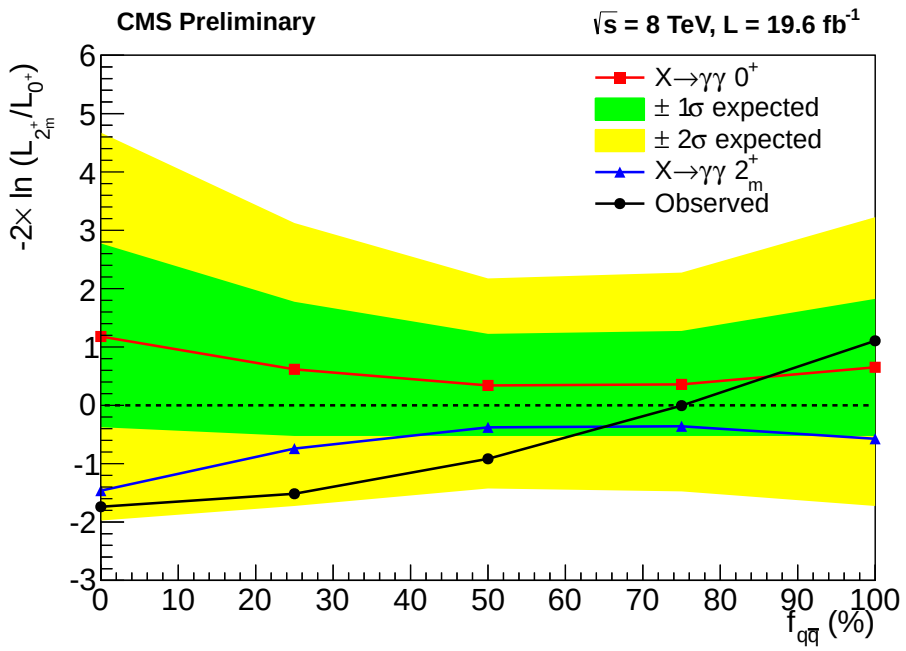

Figure 9: The distribution of the test statistic for pseudo experiments thrown under the SM, 0^+, hypothesis (red) and the *graviton-like*, 2^+_m, hypothesis (blue) as a function of the fraction of $q\bar{q}$ production relative to gg production. The observed distribution in the data is shown by the black points.

References

[1] CMS Collaboration, "Observation of a new boson at a mass of 125 GeV with the CMS experiment at the LHC", *Phys. Lett. B* **716** (2012) 30–61.

[2] ATLAS Collaboration, "Observation of a New Particle in the Search for the Standard Model Higgs Boson with the ATLAS Detector at the LHC", *Phys.Lett.* **B716** (2012) 1–29.

[3] F. Englert and R. Brout, "Broken symmetry and the mass of gauge vector mesons", *Phys. Rev. Lett.* **13** (1964) 321, doi:10.1103/PhysRevLett.13.321.

[4] P. W. Higgs, "Broken symmetries, massless particles and gauge fields", *Phys. Lett.* **12** (1964) 132, doi:10.1016/0031-9163(64)91136-9.

[5] P. W. Higgs, "Broken symmetries and the masses of gauge bosons", *Phys. Rev. Lett.* **13** (1964) 508, doi:10.1103/PhysRevLett.13.508.

[6] G. S. Guralnik, C. R. Hagen, and T. W. B. Kibble, "Global conservation laws and massless particles", *Phys. Rev. Lett.* **13** (1964) 585, doi:10.1103/PhysRevLett.13.585.

[7] P. W. Higgs, "Spontaneous symmetry breakdown without massless bosons", *Phys. Rev.* **145** (1966) 1156, doi:10.1103/PhysRev.145.1156.

[8] T. W. B. Kibble, "Symmetry breaking in non-Abelian gauge theories", *Phys. Rev.* **155** (1967) 1554, doi:10.1103/PhysRev.155.1554.

[9] CMS Collaboration, "Updated measurements of the Higgs-like boson at 125 GeV in the two photon decay channel", *CDS Record* **1530524** (2013).

[10] N. Craig and S. Thomas, "Exclusive Signals of an Extended Higgs Sector", *JHEP* **1211** (2012) 083, doi:10.1007/JHEP11(2012)083, arXiv:1207.4835.

[11] P. Ferreira et al., "Mass-degenerate Higgs bosons at 125 GeV in the Two-Higgs-Doublet Model", doi:10.1103/PhysRevD.87.055009, arXiv:1211.3131.

[12] J. F. Gunion, Y. Jiang, and S. Kraml, "Diagnosing Degenerate Higgs Bosons at 125 GeV", *Phys.Rev.Lett.* **110** (2013) 051801, doi:10.1103/PhysRevLett.110.051801, arXiv:1208.1817.

[13] Y. Grossman, Z. Surujon, and J. Zupan, "How to test for mass degenerate Higgs resonances", *JHEP* **1303** (2013) 176, doi:10.1007/JHEP03(2013)176, arXiv:1301.0328.

[14] L. D. Landau, "On the angular momentum of a two-photon system", *Dokl. Akad. Nauk. Ser. Fiz.* **60** (1948) 207.

[15] C. N. Yang, "Selection Rules for the Dematerialization of a Particle Into Two Photons", *Phys. Rev.* **77** (1950) 242.

[16] Y. Gao et al., "Spin determination of single-produced resonances at hadron colliders", *Phys. Rev. D* **81** (2010) 242–245.

[17] J. C. Collins and D. E. Soper, "Angular distribution of dileptons in high-energy hadron collisions", *Phys. Rev. D.* **16** (1977) 2219–2225.

[18] CMS Collaboration, "The CMS experiment at the CERN LHC", *JINST* **3** (2008) S08004, doi:10.1088/1748-0221/3/08/S08004.

[19] CMS Collaboration, "Electromagnetic calorimeter calibration with 7 TeV data", *CDS Record* **1279350** (2010).

[20] GEANT4 Collaboration, "GEANT4: A Simulation toolkit", *Nucl. Instrum. Meth. A* **506** (2003) 250, doi:10.1016/S0168-9002(03)01368-8.

[21] A. Hoecker et al., "TMVA: Toolkit for Multivariate Data Analysis", *PoS* **ACAT** (2007) 040, arXiv:physics/0703039.

[22] CMS Collaboration, "Measurement of the inclusive W and Z production cross sections in pp collisions at $\sqrt{s} = 7$ TeV with the CMS experiment", *JHEP* **2011** (2011) 1, doi:10.1007/JHEP10(2011)132.

[23] CMS Collaboration, "CMS Luminosity Based on Pixel Cluster Counting - Summer 2012 Update", *CDS Record* **1482193** (2012).

[24] LHC Higgs Cross Section Working Group Collaboration, "Handbook of LHC Higgs Cross Sections: 1. Inclusive Observables", CERN Report CERN-2011-002, (2011).

[25] M. Botje et al., "The PDF4LHC Working Group Interim Recommendations", (2011). arXiv:1101.0538.

[26] S. Alekhin et al., "The PDF4LHC Working Group Interim Report", (2011). arXiv:1101.0536.

[27] H.-L. Lai et al., "New parton distributions for collider physics", *Phys. Rev. D* **82** (2010) 074024, doi:10.1103/PhysRevD.82.074024.

[28] A. Martin et al., "Parton distributions for the LHC", *Eur. Phys. J. C* **63** (2009) 189, doi:10.1140/epjc/s10052-009-1072-5.

[29] NNPDF Collaboration Collaboration, "Impact of Heavy Quark Masses on Parton Distributions and LHC Phenomenology", (2011). arXiv:1101.1300.

[30] S. Frixione and B. R. Webber, "Matching NLO QCD computations and parton showers simulations", *JHEP* **0206** (2002) 029, doi:10.1088/1126-6708/2002/06/029.

[31] J. M. Campbell and R. Ellis, "MCFM for the Tevatron and the LHC", *Nucl.Phys.Proc.Suppl.* **205-206** (2010) 10–15, doi:10.1016/j.nuclphysbps.2010.08.011, arXiv:1007.3492. Talk presented by R.K Ellis at Loops and Legs in Quantum Field Theory 2010, Woerlitz, Germany, April 25-30, 2010, (6 pages and 4 figures).

[32] M. Guzzi et al., "CT10 parton distributions and other developments in the global QCD analysis", arXiv:1101.0561.

[33] G. Feldman and R. Cousins, "Unified approach to the classical statistical analysis of small signals", *Phys. Rev. D* **57** (1998) 3873–3889, doi:10.1103/PhysRevD.57.3873.

[34] S. Alioli et al., "NLO Higgs boson production via gluon fusion matched with shower in POWHEG", *JHEP* **04** (2009) 002, doi:10.1088/1126-6708/2009/04/002.

[35] P. Nason and C. Oleari, "NLO Higgs boson production via vector-boson fusion matched with shower in POWHEG", *JHEP* **02** (2010) 037, doi:10.1007/JHEP02(2010)037.

[36] T. Sjöstrand, S. Mrenna, and P. Z. Skands, "PYTHIA 6.4 Physics and Manual", *JHEP* **0605** (2006) 026, doi:10.1088/1126-6708/2006/05/026.

[37] LHC Higgs Cross Section Working Group Collaboration, "Handbook of LHC Higgs Cross Sections: 2. Differential Distributions", technical report, (2012).

[38] G. Cowan et al., "Asymptotic formulae for likelihood-based tests of new physics", *Eur. Phys. J. C* **71** (2011) 1, doi:10.1140/epjc/s10052-011-1554-0, arXiv:1007.1727.

A Background and data distributions

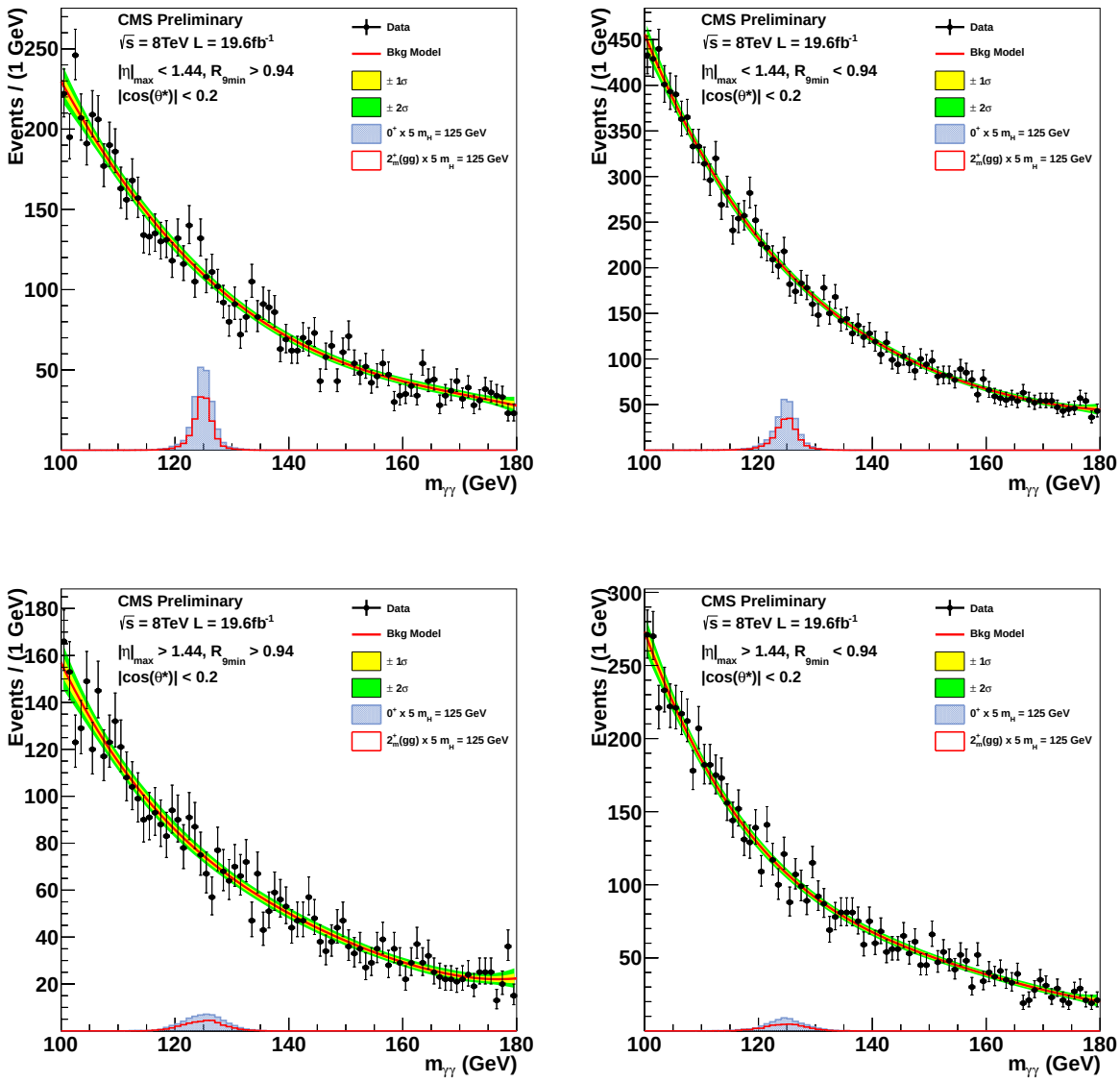

Figure 10: Background model fit for the categories with $|\cos(\theta^*_{\mathrm{CS}})| < 0.2$

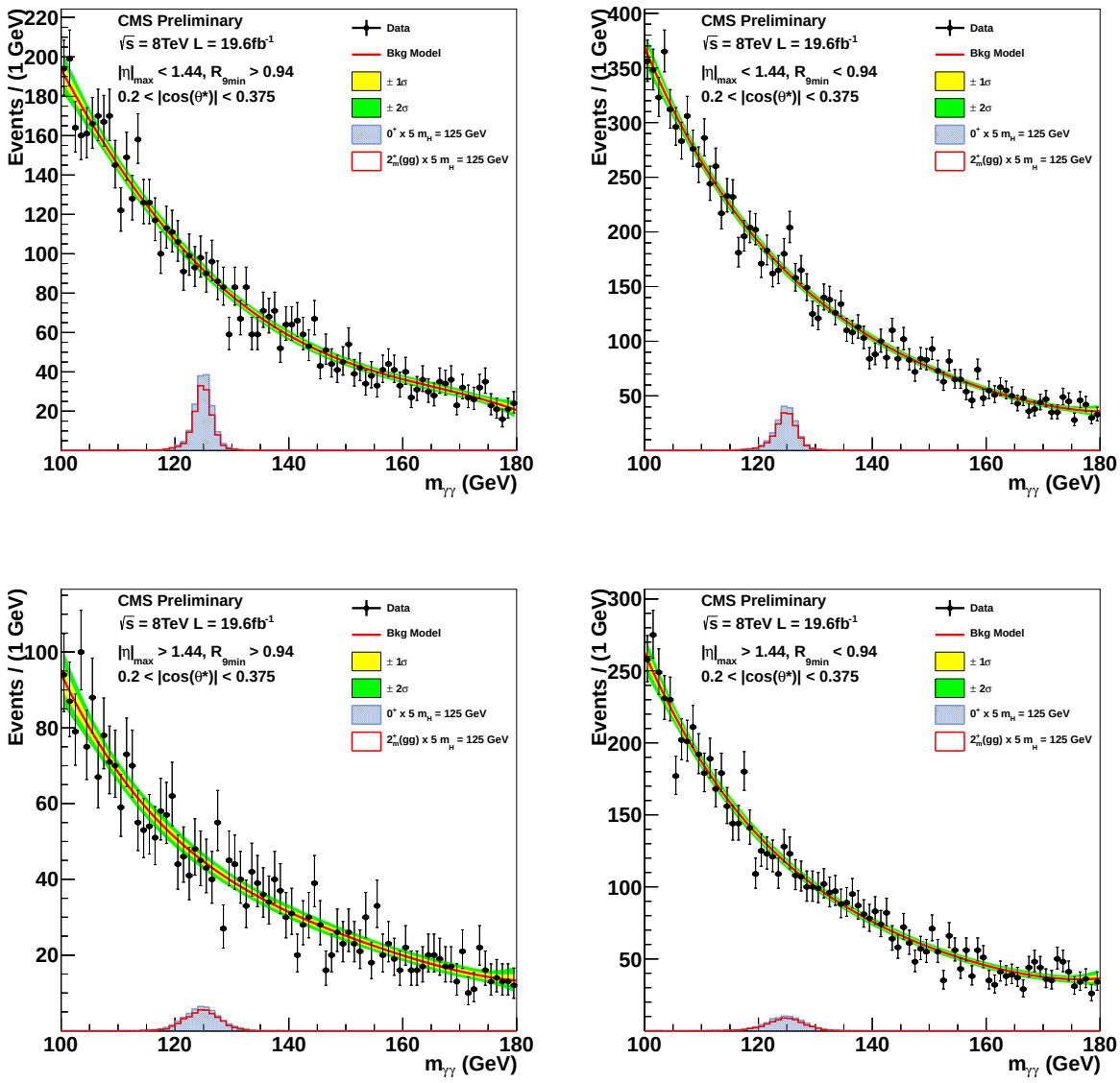

Figure 11: Background model fit for the categories with $0.2 \leq |\cos(\theta^*_{CS})| < 0.375$

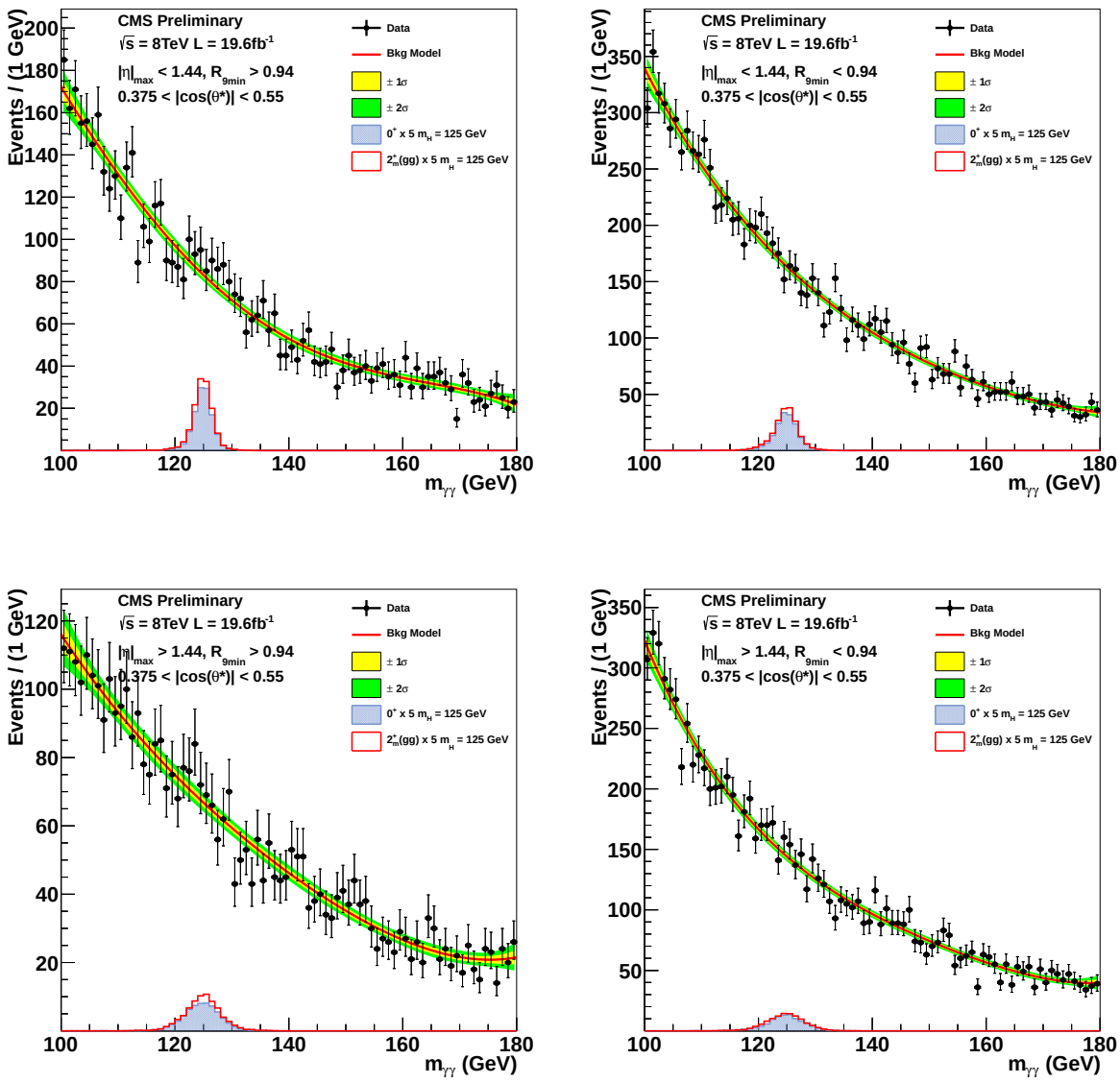

Figure 12: Background model fit for the categories with $0.375 \leq |\cos(\theta^*_{\mathrm{CS}})| < 0.55$

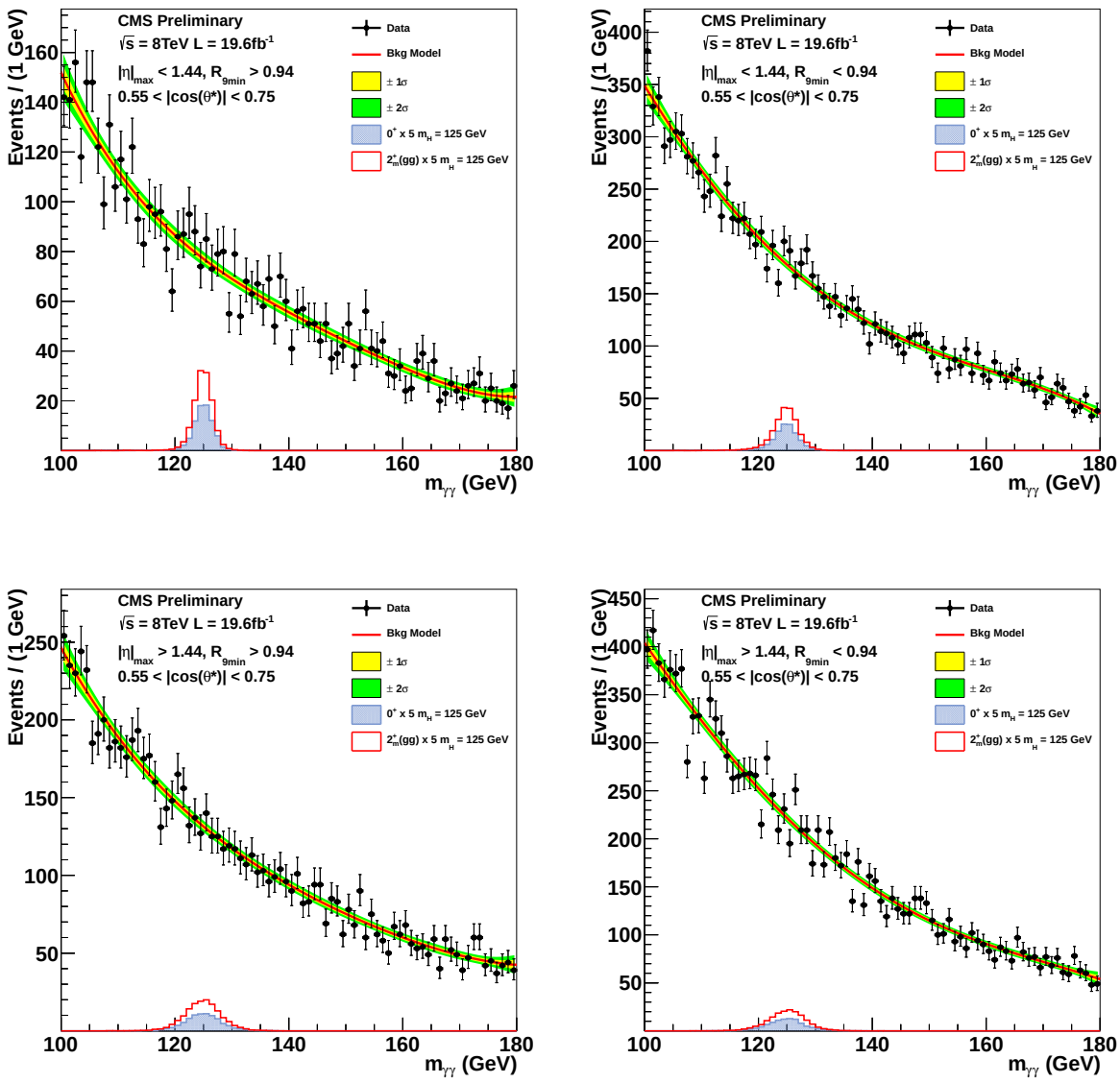

Figure 13: Background model fit for the categories with $0.55 \leq |\cos(\theta^*_{\rm CS})| < 0.75$

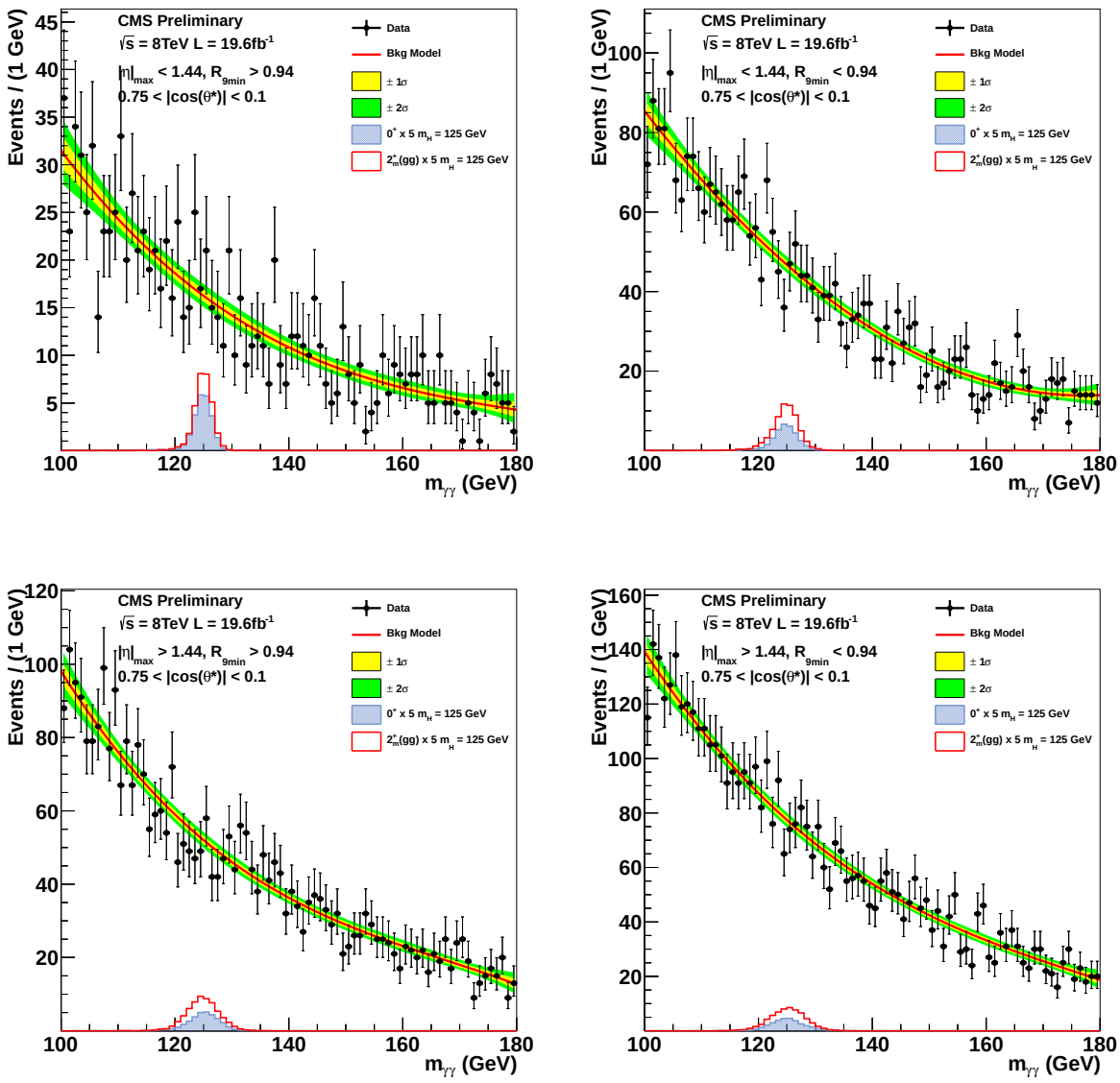

Figure 14: Background model fit for the categories with $0.75 \leq |\cos(\theta^*_{\rm CS})| < 1.0$

B Spin model fits to data

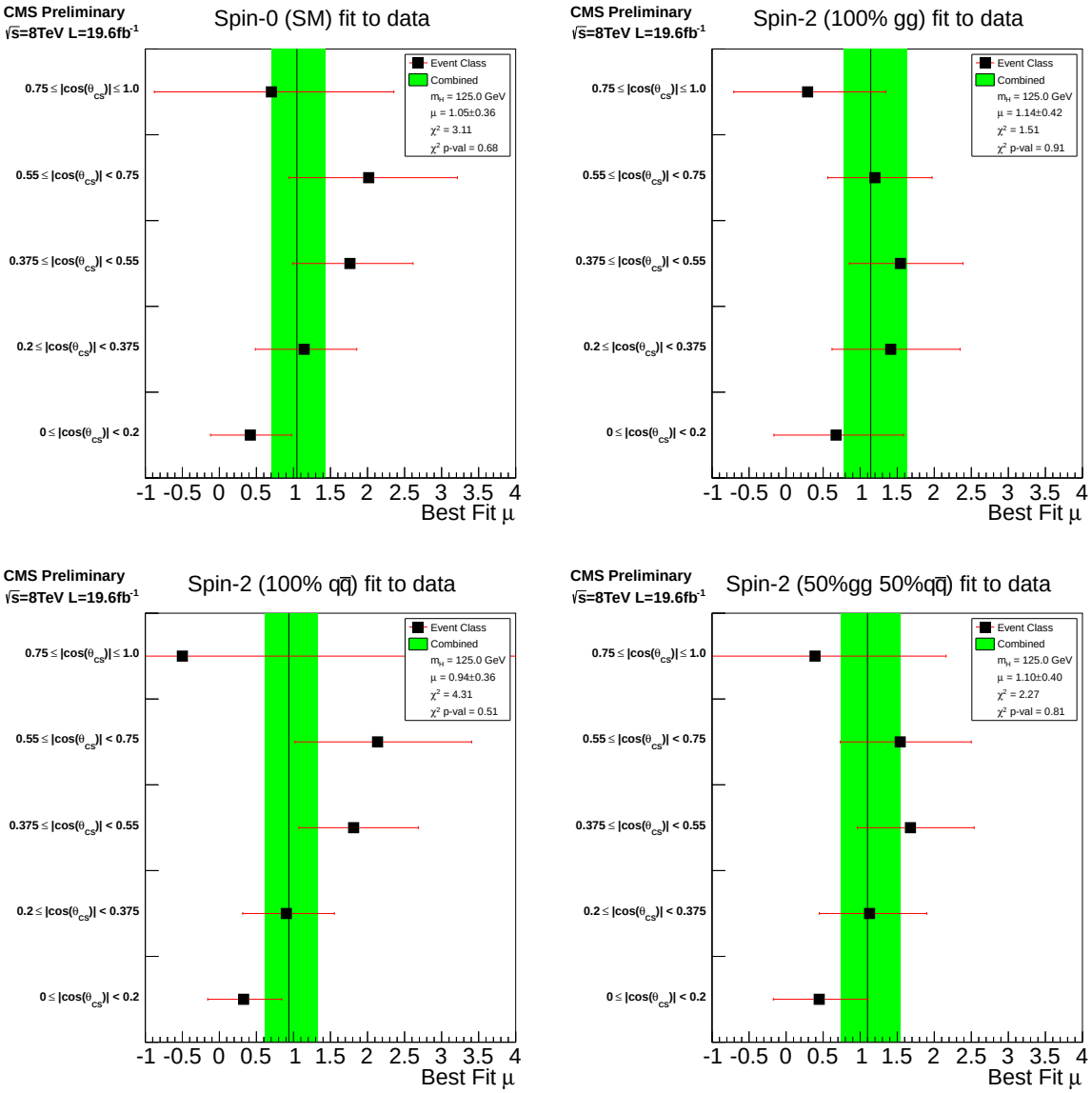

Figure 15: A fit to the data of the 0^+ model (top left), the 2^+_m (100% gg production) (top right), the 2^+_m (100% $q\bar{q}$ production) (bottom left) and the 2^+_m (50% gg, 50% $q\bar{q}$) (bottom right) in the spin analysis. The points show the fit in each $|\cos(\theta^*_{\mathrm{CS}})|$ bin (where low bin numbers correspond to small $|\cos(\theta^*_{\mathrm{CS}})|$) with the overall fit shown as the green band.

C Test statistic distributions

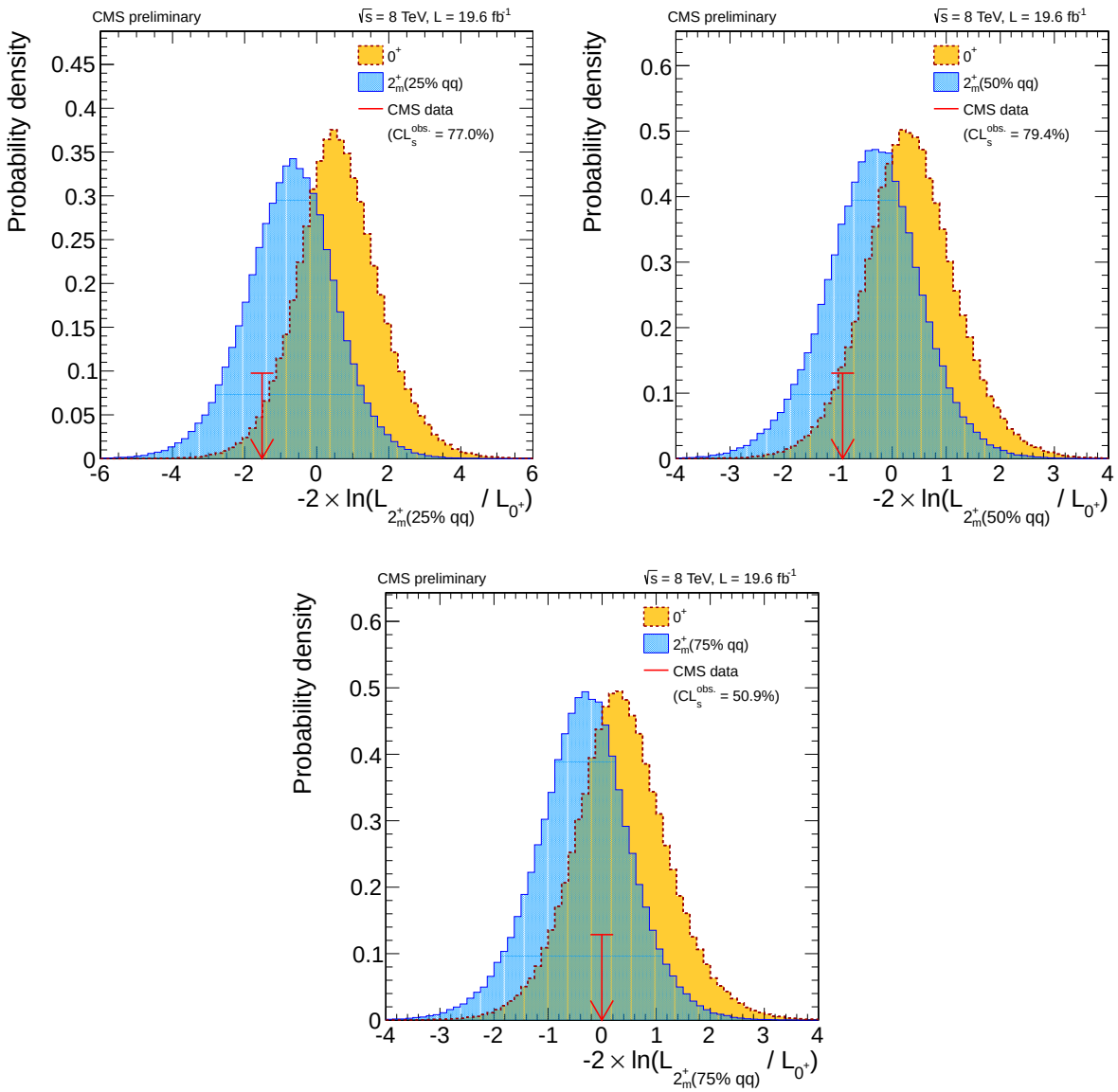

Figure 16: The distribution of the test statistic for pseudo experiments generated under the SM, 0^+, hypothesis (orange) and the *graviton-like*, 2^+_m, hypothesis (blue) with 25% $q\bar{q}$ production (top left), 50% (top right) and 75% (bottom). The observed value in the data is shown as the red arrow.